

Conceptual Design of a Proton Computed Tomography System for Applications in Proton Radiation Therapy

Reinhard Schulte, Vladimir Bashkirov, Tianfang Li, Zhengrong Liang, Klaus Mueller, Jason Heimann, Leah R. Johnson, Brian Keeney, Hartmut F.-W. Sadrozinski, Abraham Seiden, David C. Williams, Lan Zhang, Zhang Li, Steven Peggs, Todd Satogata, and Craig Woody

Abstract—Proton computed tomography (pCT) has the potential to improve the accuracy of dose calculations for proton treatment planning, and will also be useful for pretreatment verification of patient positioning relative to the proton beam. A design study was performed to define the optimal approach to a pCT system based on specifications for applications in proton therapy. Conceptual and detailed design of a pCT system is presented; the system consists of a silicon-based particle tracking system and a crystal calorimeter to measure energy loss of individual protons. We discuss the formation of pCT images based on the reconstruction of volume electron density maps and the suitability of analytic and statistical algorithms for image reconstruction.

I. INTRODUCTION

PROTON radiation has many proven advantages in radiation therapy due to its capability to deliver high doses to well-defined tumors or other targets close to critical normal structures. For proton therapy to be successful, the range of protons in tissue must be accurately known. Up to now, proton dose calculations have been performed using X-ray computed tomography (xCT). However, the accuracy of xCT for proton treatment planning is limited due to the difference in physical interactions between photons and protons, which partially obviates the advantage of proton therapy. Additional advantages of applying proton computed tomography (pCT) in proton therapy include the possibility of verifying the correct delivery of a proton treatment plan while the patient is in the treatment position. This paper reports 1) on the results of a design study for the development of pCT for applications in proton treatment, 2) phantom pCT reconstructions with a standard filtered back-projection algorithm using simulated pCT data sets calculated with GEANT4, and 3) some practical

Manuscript received October 29, 2003. This work was supported by USPHS under Grant CA46295 and by the National Medical Technology Testbed (NMTB) under the U.S. Army Medical Research Acquisition Activity DAMD17-97-2-7016. The views and conclusions contained in this paper are those of the authors and do not necessarily reflect the position or the policy of the U.S. Army or NMTB.

R. Schulte and V. Bashkirov are with Loma Linda University Medical Center, Loma Linda, CA 92354 USA (e-mail: rschulte@dominion.llumc.edu).

T. Li, Z. Liang, and K. Mueller are with the State University of New York Stony Brook, Stony Brook, NY 11790 USA.

J. Heimann, L. R. Johnson, H. F.-W. Sadrozinski, A. Seiden, D. C. Williams, and L. Zhang are with the Santa Cruz Institute for Particle Physics, University of California, Santa Cruz, Santa Cruz, CA 95064 USA.

Z. Li, S. Peggs, T. Satogata, and C. Woody are with the Brookhaven National Laboratory, Upton, NY 11973 USA.

Digital Object Identifier 10.1109/TNS.2004.829392

TABLE I
DESIGN SPECIFICATIONS FOR A pCT SCANNER FOR
THERAPEUTIC APPLICATIONS

Category	Parameter	Value
Proton source	Energy	~200 MeV (head) ~250 MeV (trunk)
	Energy spread	~ 0.1%
	Beam intensity	$10^3 - 10^7$ protons/sec
Accuracy	Spatial resolution	< 1 mm
	Electron density resolution	< 1%
Time Efficiency	Installation time	< 10 min
	Data acquisition time	< 5 min
	Reconstruction time	< 15 min (treatment planning) < 5 min (dose verification)
Reliability	Detector radiation hardness	> 1000 Gy
	Measurement stability	< 1%
Safety	Maximum dose per scan	< 5 cGy
	Minimum distance to patient surface	10 cm

considerations for implementing pCT reconstruction algorithms with hardware acceleration schemes.

II. DESIGN SPECIFICATIONS

The requirements for a pCT system designed for applications in proton therapy are dictated by the needs for accurate and safe proton beam delivery. The system must be integrated into a medical environment and, therefore, meet certain safety and practical constraints. The design specifications of a pCT scanner for applications in proton therapy are presented in Table I.

The protons used for imaging must have sufficient energy to penetrate the body part to be imaged. According to the NIST PSTAR database [1], the continuous slow-down approximation (CSDA) range of 200 MeV protons in A150 tissue equivalent plastic is 25.8 cm, which is sufficient to penetrate an adult human skull (nominal width of 20 cm in anterior posterior direction). For 250 MeV protons, the range in A150 is 37.7 cm, sufficient to penetrate an adult trunk (nominal width of 34 cm, excluding arms). In order to meet the specified accuracy on

electron density resolution, the energy should be stable to within 0.1% or 0.25 MeV for a proton energy of 250 MeV.

The spatial and electron density resolutions of a pCT scanner are physically limited by multiple Coulomb scattering (MCS) and energy loss straggling. The spatial and energy uncertainties of the pCT system should be considerably smaller than those imposed by the physical limitations, in order not to compromise the overall performance of the CT system. A clinically meaningful spatial resolution for therapy with protons is about 1 mm. This resolution value is related to what is achievable in terms of target localization and patient positioning accuracy, and is also matched by the steepness of the lateral and distal fall-off of the high-dose region. For example, in radiosurgery applications, where large doses of radiation are delivered to intracranial targets that are often within a few millimeters of critical normal structures at risk, dose localization accuracy requirements of the order of 1 mm are usually cited [2]. The electron density resolution requirement is closely related to the need of a spatial resolution of 1 mm. In order to place the distal edge of a proton beam with 10 cm range with 1 mm (1%) accuracy, one needs to know the density of each tissue voxel along the beam path with better than 1% accuracy. Human observer perception of tissue density differences of about 1% is also important in order to assist the physician in identifying tissue structures for treatment planning and verification purposes. Density differences between various soft tissues are typically in the 0.5% to 1% range [3].

A time-efficient pCT system must have a short installation, calibration, scanning, and removal time. Installation and removal of the system may be required if the detectors are not sufficiently radiation hard to stay in the beam line permanently. The time required for scanning a patient for a treatment planning study, including installation and removal of a nonpermanent system, should not be longer than 15 min (excluding image reconstruction time). When the system is used as an on-line position and dose verification system during a treatment session, fast image reconstruction within about 5 min is an essential requirement.

Detectors should be sufficiently radiation hard to maintain their function to within 1% of specified performance values for at least one year, ideally for 5 years or more. Furthermore, the system should be relatively insensitive to changes in temperature, humidity, and magnetic fields present in the treatment room.

A reasonable compromise between the dose delivered and the accuracy of electron density determination must be found, tailored to the clinical situation. The typical dose delivered by existing CT scanners during a scan for treatment planning purpose (3–5 cGy) may serve as a benchmark, and should not be exceeded by the pCT scan under similar conditions. If the scanner is used for pretreatment verification, the dose per scan times the number of treatment sessions should not exceed this benchmark value. Thus, the density resolution for treatment verification would be lower than that for treatment planning.

III. pCT HARDWARE DESIGN

A. Concept

The proposed approach to single-proton-tracking CT is illustrated in Fig. 1. The object is traversed by a broad (ideally, but

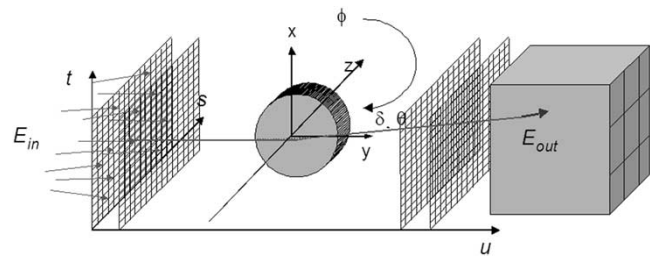


Fig. 1. Schematic of the proposed approach to pCT. Protons with known entry energy E_{in} are recorded one by one in the detector reference system (s, t, u) as they traverse the image object from many different projection angles ϕ . The recorded data include entry and exit positions and entry and exit angles as well as exit energy E_{out} in the energy detector.

not necessarily parallel) beam of protons of known energy E_{in} . A proton-tracking detector is arranged on both sides of the patient, which records the entrance and exit points and angles of individual protons. Protons are stopped in a scintillator array to measure their energy. Technical considerations for these components of the pCT system will be presented below.

B. Proton Tracking System

To determine the most likely proton path, entry and exit points as well as directions must be measured with a spatial accuracy better than the image pixel size (1 mm \times 1 mm). This requires pairs of two-dimensional (2-D) position-sensitive tracking systems on both sides of the patient. In order to keep the scanning time reasonably short, the particle tracking system should be able to detect individual protons at rates of 1 MHz or higher. Several technical solutions are possible, including gas-based detectors, silicon (Si) detectors, and scintillating fibers. Si detectors, now widely used as vertex detectors in high-energy physics, are the preferred choice for pCT because of their unrivaled spatial resolution at high event rates.

There are two major Si detector structures for tracking applications: Si strip detectors (SSD) and Si pixel detectors (SPD). For 2-D position sensitivity (X-Y), double-sided SSD (D-SSD) and pixel detectors are the most frequently used detector structures for tracking purposes. The advantages of D-SSD are: 1) 2-D position sensitivity; 2) minimum readout channel number ($\sim 2N$, N being the strip number on one side); 3) minimum radiation length (because only one wafer is used for 2-D position sensitivity); and 4) fast charge collection time (< 50 ns). There are some major disadvantages for D-SSD, however: 1) the two-sided manufacturing process is about 3–4 times more complicated and expensive than the single-sided process; 2) the detector is relatively radiation soft, due to the complicated structure on the n-side; 3) there is an ambiguity problem when a strip is hit by two or more protons simultaneously; and 4) two polarities of readout electronics are required. The maximum rate of D-SSD is limited by the charge collection time, the multihit ambiguity problem, and the shaping time in readout electronics. With fast shaping time, the rate can be 1–10 MHz per detector chip, which would be sufficient. The maximum detector chip size is limited by the maximum wafer size in the high-resistivity detector industry, which is currently at 150 mm diameter, resulting in a maximum chip size of about

10.6 cm \times 10.6 cm. Therefore, a modular design is needed to cover a larger anatomical area.

The advantages of SPD are: 1) 2-D position sensitivity; 2) single-sided process; 3) *no* multihit ambiguity; and 4) fast charge collection time (50 ns). The main disadvantages of SPD are: 1) large readout electronic channel number ($\sim N^2$, N being the number of rows or columns); 2) complicated and difficult bumper bonding technology for interconnections between the detector chip and readout electronics chip; 3) additional radiation length in the readout electronics chip; 4) position resolution limited by the minimum size of bumper bonding pads to $>20 \mu\text{m}$ (not critical for our application); and 5) high overall cost due to the large number of electronic channels and cost of bumper bonding. The maximum rate and detector chip size of SPD are similar to that of SSD.

A novel detector structure, called Si stripixel detector (SSPD), was recently developed at BNL [4] and would be suitable for the purpose of pCT. In the SSPD structure, each pixel is divided into an X- and Y-cell, which are connected and read out by projective X and Y strips, respectively. To get 2-D position sensitivity, it is essential that for each proton hit the resulting charge is shared between the X-cell and the Y-cell in a given pixel. Since the charge spreads during the drifting time (tens of nanoseconds) due to the diffusion process, the charge cloud has a finite size of approximately $20 \mu\text{m}$. In order to get charge sharing between the X-cell and the Y-cell, each pixel should be divided in such a way that the cells are interleaved with maximum distance between the two parts ($<20 \mu\text{m}$) [4]. The main advantage of the novel SSPD is that it achieves 2-D position sensitivity with the simpler single-sided process. Thus, it combines the advantages of both SSD and SPD technology. The remaining, although not limiting, disadvantage is that it is essentially a strip layout, i.e., it has the same multihit ambiguity as the D-SSD.

C. Energy Detector

The residual energy of protons traversing the image object is the single most important quantity in pCT. The accuracy of this measurement determines the density resolution of the pCT method. Although one may contemplate using the position sensitive Si detectors to determine the residual energy via dE/dx measurements in the depletion layer of these detectors, this method is inherently inaccurate due to the weak dependence of stopping power on proton energy. Therefore, a separate energy detector is required.

To measure the residual energy of a single proton with better than 1% accuracy using a compact detector is not trivial. Several solutions have been suggested, such as magnetic spectrometers [5] or a range telescope [6]. Another possibility to measure energy is a calorimeter consisting of a single or multiarray of crystal scintillators, which convert radiation-induced ionizations into scintillation light, collected by photomultiplier tubes or large-area photodiodes. Photodiodes would be preferable in the case of pCT because they are not as sensitive to the magnetic fields present in the proton gantry. Calorimeters have been widely used during the last decade for charged particle detection and identification in experiments where good energy resolution is an essential requirement (see [7]–[10] and references therein).

TABLE II
CHARACTERISTICS OF CRYSTAL SCINTILLATORS SUITABLE FOR
pCT APPLICATIONS

Parameter	CsI (pure)	Bi ₄ Ge ₃ O ₁₂ (BGO)	Lu ₂ SO ₅ :Ce (LSO)
Density (g/cm ³)	4.51	7.13	7.4
Range (cm) of 250 MeV protons	14.9	9.0	8.4
Refractive index	1.8	2.2	1.82
Radiation hardness	good	modest	good
Decay time (ns)			
fast	10-36	300	40
slow	1000		
Light output ^a			
fast	0.1	0.15	0.65
slow	0.02		

^a relative to NaI

Many options for scintillating crystals exist. Table II compares the physical characteristics of three types of crystal scintillators. The statistical uncertainty of the calorimeter output arises from the variation of photoelectron production for a given quantum efficiency. The light yield of virtually all crystal scintillators is sufficient to give a statistical contribution to the energy resolution of less than 1% for 200 MeV protons. To achieve this resolution, one needs a minimum of 10^4 photoelectrons, which, with reasonable light collection efficiency and quantum efficiency of the readout device, can be easily achieved with any of the scintillators under consideration. Due to its high density, fast decay, and high light yield, LSO may be preferred for pCT application.

IV. IMAGE RECONSTRUCTION

A. Physics of Proton Image Formation

The pCT reconstruction problem differs in some respects from that of xCT, PET, and SPECT, and requires new approaches [11], although some of the underlying principles are the same. In xCT, data collection is usually considered as the Radon transform of the object source function. In this case, the object data represent the attenuation coefficient map and the projection data the log values of the detected X-ray counts.

The main goal of pCT for therapy applications is to determine the volume electron density, ρ_e , by measuring the energy loss of protons after traversing the object. Ionization and atomic excitation are the main processes for the energy loss of protons. The mean rate of the loss per unit track length, i.e., the stopping power, is given by the Bethe–Bloch equation

$$-\frac{dE}{dx}(\mathbf{r}) = \eta_e(\mathbf{r})F(I(\mathbf{r}), E(\mathbf{r})) \quad (1)$$

where $\eta_e(\mathbf{r})$ is the electron density relative to water, \mathbf{r} represents the spatial location, $I(\mathbf{r})$ is the mean ionization potential of the medium, $E(\mathbf{r})$ is the proton energy, which changes with \mathbf{r} as the proton travels through the body, and F is a known function of I

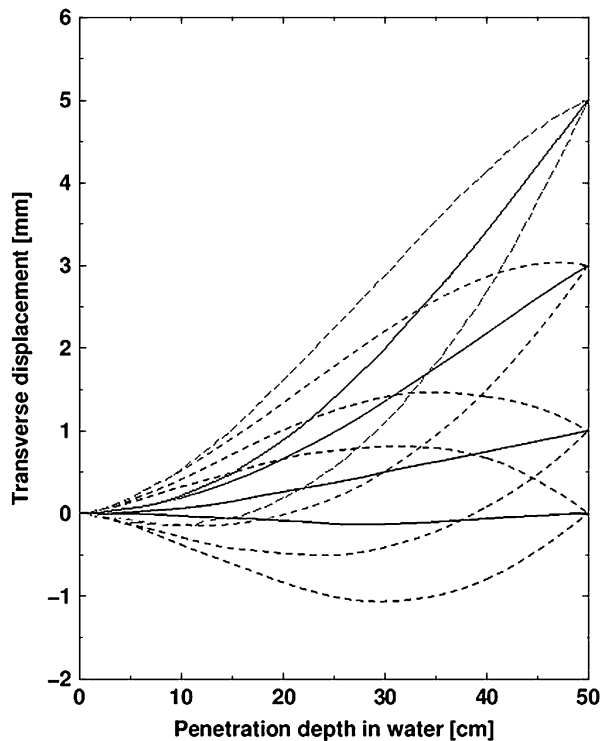


Fig. 2. Monte Carlo (MC) simulated tracks of 500 MeV protons traversing an object of water density with 50 cm diameter. The solid lines correspond to the most likely path of protons with an exit displacement of 0, 1, 3, and 5 mm, while the dashed lines represent the one-sigma envelopes caused by MCS.

and E defined by the Bethe–Bloch equation [12]. With reasonable assumptions and approximations, the nonlinear differential equation (1) can be integrated as

$$\int_{E_{\text{in}}}^{E_{\text{out}}} \frac{dE}{F(I_{\text{water}}, E)} = \int_L \eta_e(\mathbf{r}) dl \quad (2)$$

which would be in the format of the Radon transform if proton paths were straight lines confined to a 2-D plane: the right side is the line integral of the relative electron density along the proton path L , and the left side is a unique function of the proton energy difference. In (2), $I(\mathbf{r})$ was replaced by the mean ionization potential of water $I_{\text{water}} = 61.77$ eV. This is justified because in human tissues the variation of I is not very large and the dependence of the function F on I is relatively weak.

In pCT, multiply scattered protons traversing the object travel along a curved zigzag path, which may deviate significantly from a straight line and is not confined to a 2-D plane (see Fig. 2). Further, protons usually are not absorbed but traverse the object completely. Thus, the photon counting rate used in X-ray CT, PET, and SPECT has to be replaced by the energy loss measurement for protons traveling along tracks L that lead to the same image pixel. Given the known proton entrance energy and the measured exit energy, the energy integral of (2) can be computed, resulting in the projection data. The image reconstruction problem for pCT is then to obtain the best estimate for the relative electron density map from the measured proton data.

B. Reconstruction Algorithms

Since proton paths are not straight lines and are not confined to a plane, the exact inversion of the pCT integral equation is

impossible. The well-established *analytical reconstruction algorithms* based on the inversion of the Radon transform, such as the filtered backprojection (FBP) algorithm, are, therefore, of limited use in pCT. On the other hand, we have shown in pCT simulation studies that the straight-line 2-D approximation can lead to pCT images with reasonable spatial and density resolution (see the next section). The FBP algorithm, which is fast and robust, may be sufficient if pCT is used for a fast reconstruction of pretreatment patient position.

In order to find a more exact solution of the object function $\eta_e(\mathbf{r})$, one may resort to *iterative, statistical reconstruction algorithms*. In general terms, the discrete data acquisition model for pCT may be expressed as

$$\begin{aligned} y_i(\Delta E, \mathbf{r}_{\text{in}}, \mathbf{r}_{\text{out}}, \Omega_{\text{in}}, \Omega_{\text{out}}) \\ = \sum_j M_{ij}(\mathbf{r}_{\text{in}}, \mathbf{r}_{\text{out}}, \Omega_{\text{in}}, \Omega_{\text{out}}) \eta_j \\ + n_i(\mathbf{r}_{\text{in}}, \mathbf{r}_{\text{out}}, \Omega_{\text{in}}, \Omega_{\text{out}}) + b_i \end{aligned} \quad (3)$$

where y_i is the integral described by the left side of (2) for the energy loss $\Delta E = E_{\text{in}} - E_{\text{out}}$, the matrix element M_{ij} is the product of the probability that a proton detected in pixel i passed the voxel j and the path length through that voxel (approximated by the voxel size), η_j is the relative electron density of the voxel j , n_i is the noise in pixel i , and b_i is the background signal of the energy detector in pixel i . The arguments $\mathbf{r}_{\text{in}}, \mathbf{r}_{\text{out}}$, and $\Omega_{\text{in}}, \Omega_{\text{out}}$ are the entry and exit positions and directions of the protons, respectively. Note that the pCT image noise, which is determined by a combination of detector measurement uncertainty and energy straggling, is more complicated than the Poisson-distributed noise in xCT, SPECT, and PET. Monte Carlo (MC) simulations of radiation transport may be the ideal tool to model the noise in pCT; however, the computing effort would be very large.

Iterative algorithms are usually based on the maximum-likelihood (ML) or the maximum *a posteriori* probability (MAP). For the Poisson noise model used in PET and SPECT, the ML expectation-maximization (ML-EM) [13], [14] and MAP-EM [15], [16] reconstruction techniques have been extensively investigated. Equivalent algorithms for pCT have yet to be developed. With the ordered subset (OS) strategy [17], the computational burden for both ML-EM and MAP-EM is acceptable, and the same strategy may be applicable to pCT reconstruction.

The ultimate approach to pCT reconstruction may be *list-mode data acquisition*, which records individual proton entrance and exit positions and directions, exit energies, and loss due to nuclear interactions as an event. The pCT image is then reconstructed from each recorded event. It is clear that this will result in the most accurate image, because the list-mode data contain the largest amount of information about the imaged object. It is also obvious that this reconstruction will consume most computing time because the reconstruction has to process each of many million events individually, rather than sorting millions of events into a few hundred projection data sets and processing each projection dataset as a group simultaneously. However, using modern hardware acceleration it is likely that reasonable reconstruction times can be achieved.

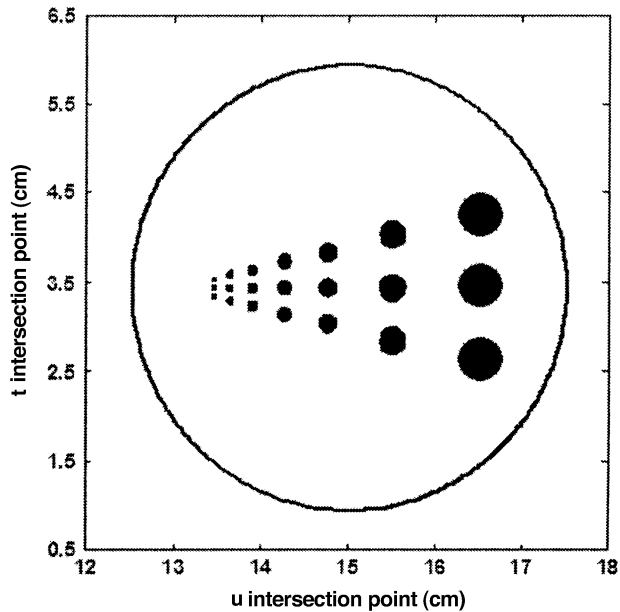


Fig. 3. Laboratory reference system for the simulations. The protons arrive along u direction at plane $u = 0$ cm. The detector is at $u = 30$ cm. The hole sizes from left to right are 0.5, 0.75, 1, 1.5, 2, 3, and 4 mm.

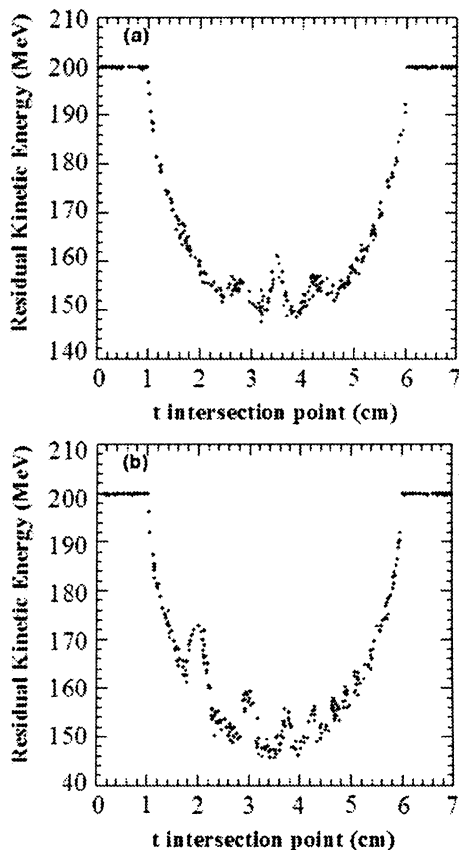


Fig. 4. Residual energy versus entry position at different views: (a) view angle 0° , (b) view angle 90° . Some phantom structures are already reflected in these one-view profiles.

V. SIMULATION RESULTS

A. Method

Simulated pCT scan data were generated by the GEANT4 MC simulation code [18]. The geometry module of GEANT4 was used to generate an aluminum disk phantom with seven

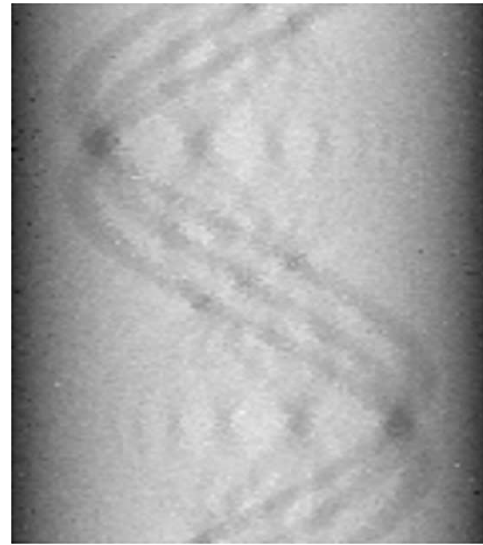


Fig. 5. Sinogram constructed by interpolation of virtual projection rays.

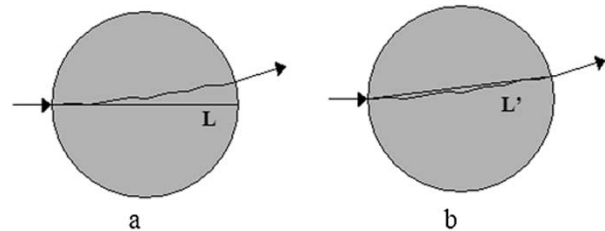


Fig. 6. Illustration of the proton path estimation. (a) When only entry position and direction of the incoming proton are known, the best approximation of the proton path within the object is straight line L . (b) Taking into account both entry and exit position one approximates the proton trajectory by straight line L' connecting entry and exit point.

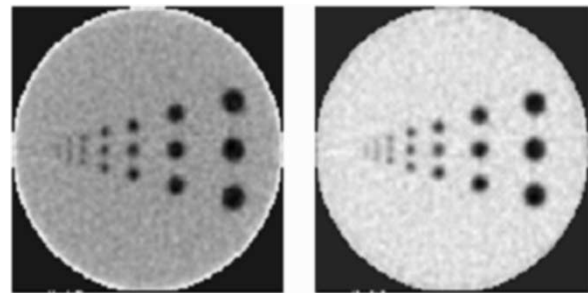


Fig. 7. Reconstructed image using paths L (left) and path L' (right) for image reconstruction. Although the spatial resolution of both images is similar, some density distortion is present in the left image at the object boundary, which is not seen in the right image.

rows of holes (Fig. 3). The diameter of the disk was 50 mm and the diameters of the holes in each row were 4, 3, 2, 1.5, 1, 0.75, and 0.5 mm, respectively. The average deflection of a 200 MeV proton in this phantom is comparable to that in a human head.

The MC program simulated the transport of 200 MeV monoenergetic protons arriving at the plane $u = 0$ cm with random heights t , ranging from $t = 0$ cm to $t = 7$ cm, and being detected at the plane $u = 30$ cm. The location and direction of exiting protons were provided by the simulation, as well as their residual energy. Typical profiles of the residual proton energy versus the initial location for 0° and 90° projections are plotted

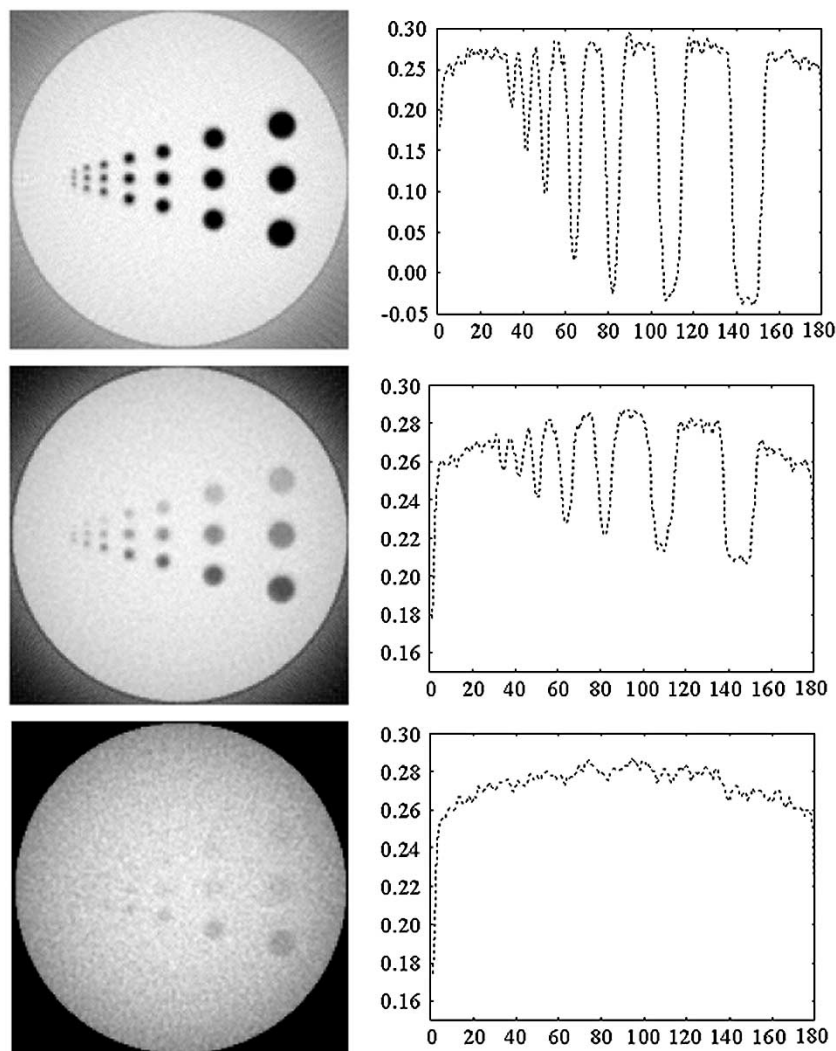


Fig. 8. Reconstructed images and horizontal profiles for different contrast phantom simulations. (Top row: high contrast, middle row: medium contrast; bottom row: low contrast.)

in Fig. 4, and a complete sinogram calculated by interpolation of the virtual projection rays is presented in Fig. 5.

B. Comparison of Reconstructions Using Different Path Estimations

To study the effect of using different path approximations we used a high-contrast scenario by filling the phantom holes with air. A full circular orbit was scanned in 2° increments, and 350 simulated proton events were generated per projection. We used two different path approximations (Fig. 6): the projection line L assumes that the proton follows its initial direction without any scattering; line L' was determined by the entry and exit positions of the proton at the detector planes, assuming that the detectors can measure both the position and direction of the exiting proton, and that the object boundary is roughly known. It is obvious that L' is generally closer to the true path of the proton than line L .

Two images reconstructed with the FBP algorithm are shown in Fig. 7. The left image was obtained using a continuation of the initial proton direction (paths L), while the right image was reconstructed using paths L' . Some difference between these two

results is seen, especially at the object boundary and for the density contrast. The reconstructed image based on the estimated paths L' is closer to the ground truth.

C. Contrast Detectability

In this simulation study, the density contrast inside the Al-disk phantom was grouped into three levels: high contrast (Al-disk and air holes); medium contrast (Al-disk and 90%, 80%, and 70% Al-density holes); and low contrast (Al-disk and 99.7%, 99%, and 97% Al-density holes). For this study, 35 000 simulated proton events were generated per projection. Reconstructed images using the virtual-ray method are shown in Fig. 8, together with energy-loss profiles along the central horizontal line. Note that the display window level for the three images is different. Even at the smallest contrast level, holes are distinguishable down to a diameter of 1.5 mm.

VI. HARDWARE ACCELERATION

Clinical utility requires fast reconstruction within minutes. This is best afforded by performing the reconstruction exploiting commodity graphics hardware boards (GPUs), which

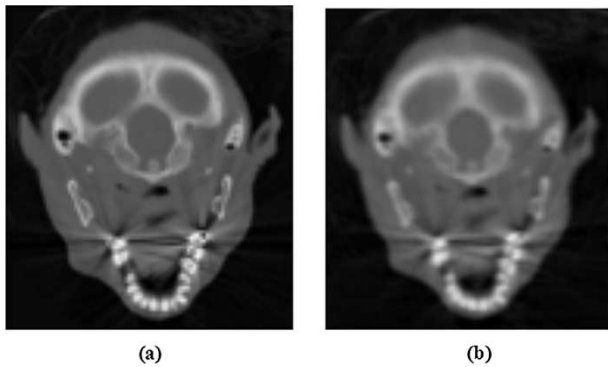


Fig. 9. CT head dataset: (a) original, (b) reconstructed from 80 high-quality simulated X-ray projections acquired from (a).

are currently evolving in their capabilities. A reconstruction is performed by using the texture mapping facilities of the hardware for performing the interpolations required in the projection and backprojection operations [19], [20]. The other arithmetic operations that occur in the reconstruction algorithms can also be performed with this hardware.

Finally, the probability envelope of the proton path can be modeled by performing a slice blurring before the projection summing or volume update during projection and back projection, respectively. In this approach, one determines the amount of blurring as a function of the width of the envelope at the slice position.

Using our hardware reconstructor, we were able to perform a cone-beam reconstruction (16° cone-angle) of a 128^3 volume from 80 projections in 3 SART iterations in 50 s, which is clearly in the clinical range. Fig. 9(b) shows a slice of the hardware-reconstructed CT head together with the original CT reconstruction Fig. 9(a).

VII. CONCLUSION

The development of pCT is desirable to improve the accuracy of planning and delivering proton radiation treatments and to fully exploit the advantages of proton therapy. A state-of-the-art pCT system should use single proton registration with Si-based track detectors and a crystal calorimeter for energy measurement. Effective iterative reconstruction algorithms, taking into account the peculiarities of proton transport through the object, have yet to be optimized and may require hardware acceleration methods in order to be suitable for clinical applications.

REFERENCES

- [1] PSTAR database, National Institute for Standards and Technology. [Online]. Available: <http://www.physics.nist.gov/PhysRefData/Star/Text/PSTAR.html>
- [2] M. H. Phillips, K. J. Stelzer, T. W. Griffin, M. R. Mayberg, and H. R. Winn, "Stereotactic radiosurgery: A review and comparison of methods," *J. Clin. Oncol.*, vol. 12, no. 5, pp. 1085–1099, 1994.
- [3] M. A. Weinstein, P. M. Duchesneau, and W. J. MacIntyre, "White and gray matter of the brain differentiated by computed tomography," *Radiology*, vol. 122, no. 3, pp. 699–702, 1977.
- [4] Z. Li, "Novel silicon stripixel detector: Concept, simulation and design," BNL, Tech. Rep. 67 527, June 2000.
- [5] Y. Takada, K. Kondo, T. Marume, K. Nagayoshi, I. Okada, and K. Takikawa, "Proton computed tomography with a 250 MeV pulsed beam," *Nucl. Instrum. Meth. A*, vol. 273, no. 1, pp. 410–422, 1988.
- [6] P. Pemler *et al.*, "A detector system for proton radiography on the gantry of the Paul-Scherrer-Institute," *Nucl. Instrum. Meth. A*, vol. 432, no. 2–3, pp. 483–495, 1999.
- [7] A. Wagner *et al.*, "Energy resolution and energy-light response of CsI(Tl) scintillators for charged particle detection," *Nucl. Instrum. Meth. A*, vol. 456, pp. 290–299, 2001.
- [8] M. Moszynski, J. Zalipska, M. Balcerzyk, M. Kapusta, W. Mengesha, and J. D. Valentine, "Intrinsic energy resolution of NaI(Tl)," *Nucl. Instrum. Meth. A*, vol. 484, pp. 259–269, 2002.
- [9] W. G. Gong *et al.*, "Resolution tests of CsI(Tl) scintillators read out by pin diodes," *Nucl. Instrum. Meth. A*, vol. 268, pp. 190–199, 1988.
- [10] J. R. M. Annand, J. C. McGeorge, G. J. Miller, V. Holliday, and L. Isaksson, "A large-solid-angle CsI(Tl) proton spectrometer," *Nucl. Instrum. Meth. A*, vol. 292, pp. 129–134, 1990.
- [11] K. Mueller *et al.*, "Reconstruction for proton computed tomography: A practical approach," presented at the 2003 IEEE Nuclear Science Symposium and Medical Imaging Conference, paper M14–342.
- [12] H. Bichsel *et al.*, *Passage of Charged Particles Through Matter*, B. H. Billings *et al.*, Eds. New York: McGraw-Hill, 1972, vol. 42, pp. 8–189. American Institute of Physics Handbook.
- [13] L. Shepp and Y. Vardi, "Maximum likelihood reconstruction for emission tomography," *IEEE Trans. Med. Imaging*, vol. MI-1, pp. 113–122, Oct. 1982.
- [14] K. Lange and R. Carson, "EM reconstruction algorithms for emission and transmission tomography," *J. Comput. Assist. Tomogr.*, vol. 8, pp. 306–316, 1984.
- [15] Z. Liang and H. Hart, "Bayesian image processing of data from constrained source distributions, I: Non-valued, uncorrelated and correlated constraints," *Bull. Math. Biol.*, vol. 49, pp. 51–74, 1987.
- [16] E. Levitan and G. Herman, "A MAP-EM algorithm for image reconstruction in emission tomography," *IEEE Trans. Med. Imaging*, vol. MI-6, pp. 185–192, Sept. 1987.
- [17] H. Hudson and R. Larkin, "Accelerated image reconstruction using ordered subsets of projection data," *IEEE Trans. Med. Imaging*, vol. 13, pp. 601–609, Dec. 1994.
- [18] S. Agostinelli *et al.*, "GEANT4—A simulation toolkit," *Nucl. Instrum. Meth. A*, vol. 506, no. 3, pp. 250–303, 2003.
- [19] F. Xu and K. Mueller, "A unified framework for rapid 3D computed tomography on Commodity GPUs," presented at the 2003 IEEE Nuclear Science Symposium and Medical Imaging Conference, paper M10–331.
- [20] K. Mueller and R. Yagel, "Rapid 3D cone-beam reconstruction with the algebraic reconstruction technique (ART) using texture mapping hardware," *IEEE Trans. Med. Imaging*, vol. 19, pp. 1227–1237, Dec. 2000.